crystals

MDPI

Article

Crystal Growth and Electronic Properties of LaSbSe

Krishna Pandey [1], Lauren Sayler [2], Rabindra Basnet [3], Josh Sakon [4], Fei Wang [2] and Jin Hu [1,3,*]

[1] Materials Science and Engineering Program, Institute for Nanoscience and Engineering, University of Arkansas, Fayetteville, AR 72701, USA
[2] Department of Chemistry & Biochemistry, Missouri State University, Springfield, MO 65897, USA
[3] Department of Physics, University of Arkansas, Fayetteville, AR 72701, USA
[4] Department of Chemistry & Biochemistry, University of Arkansas, Fayetteville, AR 72701, USA
* Correspondence: jinhu@uark.edu

Abstract: The ZrSiS-type materials have gained intensive attentions. The magnetic version of the ZrSiS-type materials, *Ln*SbTe (*Ln* = Lanthanide), offers great opportunities to explore new quantum states owing to the interplay between magnetism and electronic band topology. Here, we report the growth and characterization of the non-magnetic LaSbSe of this material family. We found the metallic transport, low magnetoresistance and non-compensated charge carriers with relatively low carrier density in LaSbSe. The specific heat measurement has revealed distinct Sommerfeld coefficient and Debye temperature in comparison to LaSbTe. Such addition of a new *Ln*SbSe selenide compound could provide the alternative material choices in addition to *Ln*SbTe telluride materials.

Keywords: topological semimetals; electronic transport; heat capacity; layered material

check for updates

Citation: Pandey, K.; Sayler, L.; Basnet, R.; Sakon, J.; Wang, F.; Hu, J. Crystal Growth and Electronic Properties of LaSbSe. *Crystals* **2022**, *12*, 1663. https://doi.org/10.3390/cryst12111663

Academic Editor: Fapeng Yu

Received: 13 October 2022
Accepted: 15 November 2022
Published: 18 November 2022

Publisher's Note: MDPI stays neutral with regard to jurisdictional claims in published maps and institutional affiliations.

Copyright: © 2022 by the authors. Licensee MDPI, Basel, Switzerland. This article is an open access article distributed under the terms and conditions of the Creative Commons Attribution (CC BY) license (https://creativecommons.org/licenses/by/4.0/).

1. Introduction

The discoveries of topological semimetals (TSMs) have created promising material platforms to study fundamental physics and develop novel device applications [1–8]. These materials host relativistic fermions with linear energy-momentum dispersions that are analogous to Dirac and Weyl fermions in the field of high energy physics [1,9]. Such Dirac and Weyl states are protected by certain symmetries, and display various exotic properties, such as large magnetoresistance [8], high mobility [8], chiral anomaly [10–13], and surface Fermi arcs [14–18]. Unlike Dirac semimetals (DSMs) and Weyl semimetals (WSMs) where the linearly dispersed bands cross at discrete points in the momentum space, the nodal semimetals (NLSMs) exhibit interesting linear band crossings along one-dimensional loops or lines. Among various NLSMs, the ZrSiS-family compounds have gained intensive attention. It is a large materials family represented by a chemical formula *WHM* (*W*= Zr/Hf/lanthanides; *H* = Si/Ge/Sn/Sb, *M* = O, S, Se,Te) [19–32]. Those compounds crystallize in a layered crystal structure, formed by the stacking of sandwich layers in which the two dimensional (2D) square net of *H*-atoms are sandwiched by *W* m layers. Many *WHM* materials possess tetragonal structures with a space group *P*4/*nmm*, while some exhibit orthorhombic distortions. Two types of Dirac states have been discovered in lots of *WHM* compounds, including the gapless Dirac point states protected by non-symmorphic symmetry, and the slightly gapped Dirac nodal-line states generated by the glide mirror symmetry [19,20,22,31,33]. Those electronic states lead to several interesting properties in *WHMs* such as the surface floating bands [34,35], enhanced electronic correlations [31,32,36], and pressure-induced topological phase transitions [37,38].

The *Ln*SbTe materials represents magnetic version of *WHM* materials [27,28,39–50]. In those compounds, the spin degree of freedom is activated when *Ln* is a magnetic rare earth element such as Ce [28,39,40], Gd [27,41,42], Nd [46,47], Sm [44,45], Ho [48,49], and Dy [50]. Various antiferromagnetic (AFM) ground states have been observed in those *Ln*SbTe compounds [27,28,44,46,48,50]. Non-trivial topology has been demonstrated in

several *Ln*SbTe compounds [27,28,44,49–51], which is predicted to be tunable by magnetism when metamagnetic transitions occurs [28]. In addition to magnetism, rich quantum phenomena such as Kondo effects [39,44,46,52], charge density waves (CDW) [40,42,43], enhanced electronic correlations [44,46,49], and possible magnetic frustration [44] have been observed in various *Ln*SbTe compounds. Such abundance of exotic quantum phenomena makes *Ln*SbTe a model platform to investigate topological physics.

In topological materials, spin-orbit coupling (SOC) is a known parameter that affects electronic states, which is relatively easily tunable by elementary substitutions. In *Ln*SbTe, replacing Te with other chalcogen elements is one possible route to vary SOC. Thus far, $CeSb(Te_{1-x}Se_x)$ [40,53] has been reported to show a complex magnetic ordering that results in a possible devil's staircase in magnetization measurements. In addition, features suggesting a Kondo lattice with a small charge carrier density has been observed in CeSbSe [53]. Extending from tellurides to selenides, those *Ln*SbSe compounds provide additional opportunities to investigate the topological materials and topological physics in *WHM* family. This motivated us to study the previously unexplored non-magnetic *WHM* compound LaSbSe in this work. We found that LaSbSe exhibits metallic behavior in electron transport, with small magnetoresistance and non-compensated charge carriers, which is distinct from the telluride compound LaSbTe.

2. Materials and Methods

The LaSbSe single crystals were synthesized by a two-step chemical vapor transport (CVT) method. First, a polycrystalline precursor was prepared by heating the stoichiometric mixture of La (99.88%, Alfa Assar), Sb (99.5%, Alfa Assar) and Se (99.999%, Alfa Assar) at 750 °C at a rate of 50 °C per hour, stayed for 2 days, and followed by cooling down to room temperature. The precursor was then used as the source material for the subsequent CVT growth with selenium tetrachloride as a transport agent. Millimeter-size rectangular crystals with metallic luster were obtained after two weeks' growth with a temperature gradient from 1000 to 850 °C, as shown in the inset of Figure 1b. Lowering temperature or shorter duration only yielded powders rather than crystals. The obtained single crystals for LaSbSe are found to be relatively softer and easy to cleave than *Ln*SbTe compounds, which is in line with the lower Debye temperature in comparison to the *Ln*SbTe compounds [39,41,44,46] as will be discussed below. The elemental composition was checked by using energy-dispersive X-ray spectroscopy (EDS). Within the resolution limit of EDS, stoichiometric composition of LaSbSe was obtained without any traces of other elements. Furthermore, the crystal structure was determined by both powder and single crystal X-ray diffraction (XRD) performed at room temperature by using Rigaku XtaLAB Synergy-S diffractometers. The powder diffraction was performed by using Cu Kα radiation on power sample obtained from grounding single crystals, and the single crystal XRD spectrum was collected by using Mo Kα radiation. The refinements of powder and single crystal XRD data were performed by JANA2006 [54]. Electronic transport and heat capacity measurements were performed by using a physical properties measurement system (PPMS).

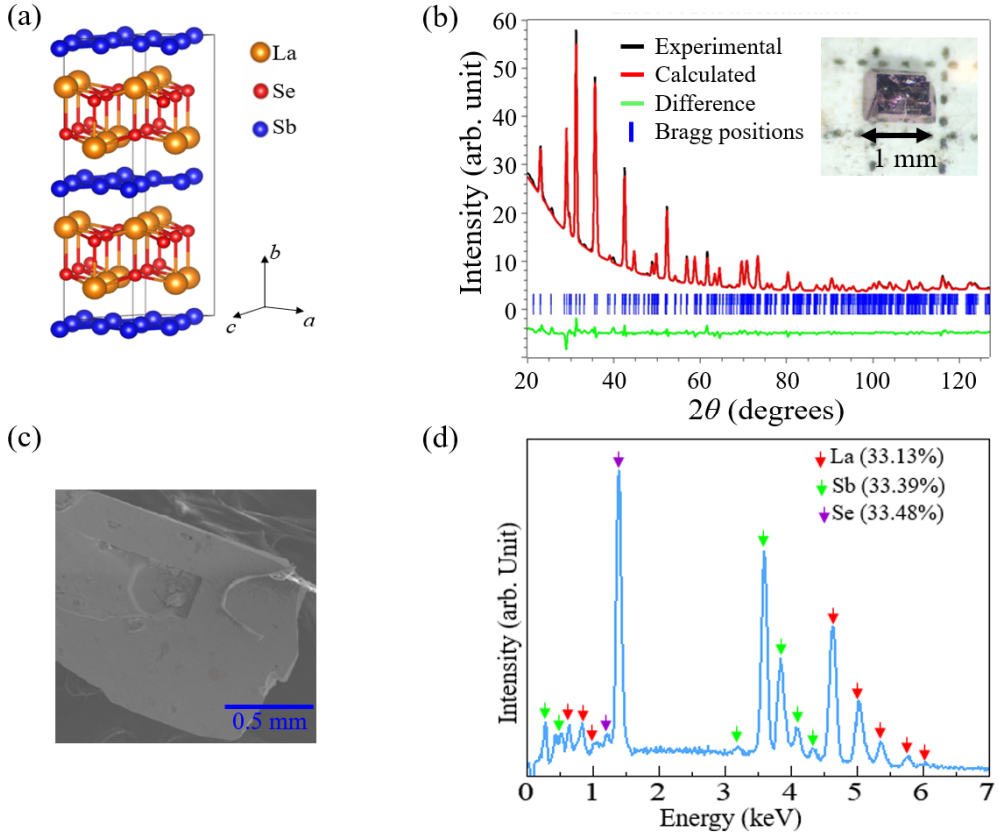

Figure 1. (**a**) Crystal structure of LaSbSe. (**b**) Powder XRD pattern and refinement for LaSbSe. Powder sample was obtained by grounding single crystals. Inset: image of a LaSbSe single crystal. (**c**) Scanning electronic microscopy (SEM) image of a LaSbSe single crystal. (**d**) Energy dispersive spectroscopy (EDS) spectrum of the LaSbSe single crystal shown in (**c**). The obtained composition is $La_{0.992}Sb_{1.000}Te_{1.003}$.

3. Results and Discussions

Stoichiometric *Ln*SbTe compounds crystallize in the tetragonal lattice with nonsymmorphic space group $P4/nmm$, in which the Sb square nets are sandwiched between the *Ln*-Te layers [28,43,45,48,50]. This Sb plane can be substituted by Te, resulting in nonstoichiometric compositions $LnSb_{1-x}Te_{1+x}$ which is accompanied by orthorhombic distortions [41,52]. In addition, vacancies in the Sb layer have also been observed in those nonstoichiometric compounds [43,45]. To resolve the crystal structure of LaSbSe, we performed both powder and single crystal XRD. The crystal structure was solved and refined from single crystal XRD, which was then used as the model structure for a Rietveld refinement with the powder diffraction pattern. The obtained crystal structure is shown in Figure 1a and the refined lattice atomic parameters are listed in Tables 1 and 2. Figure 1b shows the powder XRD spectrum and refinement. The refined crystal structure of LaSbSe is a distorted variant of the $P4/nmm$ structure of *Ln*SbTe. It is pseudo-tetragonal but the Sb square net is distorted, rendering from which a monoclinic structure with a space group of $P21/c$ can be determined for our LaSbSe. The structure parameters are summarized in Table 1. Compared to a previous report on LaSbSe [55], our refined structure is consistent in space group and atomic positions but evidently different in lattice parameters. A stoichiometric composition, LaSbSe, was also obtained from the structure refinement, which is consistent with the composition analysis using EDS. The scanning electron microscopy (SEM) image of a LaSbSe single crystal and the corresponding EDS spectrum are shown in Figure 1c,d. To further confirm the structure of LaSbSe, we have also resolved the structure using single crystal XRD, from which a consistent crystal structure was obtained as shown in Table 2.

Table 1. Room temperature crystal structure determined by powder XRD. Space group: $P21/c$. a = 4.24437 (17) Å, b = 18.4271 (4) Å, c = 6.0175 (4) Å. β = 134.971 (4)°. R_p = 0.023, R_{wp} = 0.032, R_{exp} = 0.349, $R(F)$ = 0.060, χ^2 = 0.008.

Atom	Wyckoff	x	y	z	U_{iso}
La	4*e*	−0.005 (8)	0.35203 (4)	0.242 (4)	0.0105 (3)
Sb	4*e*	0.498 (4)	−0.00386 (14)	0.750 (3)	0.0039 (3)
Se	4*e*	−0.006 (11)	0.18612 (7)	0.237 (4)	0.0080 (6)

Table 2. Room temperature crystal structure determined by single crystal XRD. Space group: $P21/c$. a = 4.2512 (1) Å, b = 18.4342 (2) Å, 6.0153 (1) Å. β = 134.978 (3)°.

Atom	Wyckoff	x	y	z	U_{iso}*/U_{eq}
La	4*e*	0.49016 (5)	0.352057 (8)	0.24017 (3)	0.00743 (11)
Sb	4*e*	0.98422 (6)	0.000418 (14)	0.23424 (3)	0.00802 (12)
Se	4*e*	0.49157 (7)	0.185065 (16)	0.24162 (4)	0.00756 (18)

In *Ln*SbTe compounds, both metallic and non-metallic electronic transport behaviors have been observed in temperature dependent resistivity measurements. For example, NdSbTe [46], CeSbTe [39], and SmSbTe [44] exhibit nonmetallic transport (i.e., increase of resistivity upon cooling) with Kondo-like features, whereas the ZrSiS metallic transport (i.e., resistivity decreases with reducing temperature) has been reported in LaSbTe [56], GdSbTe [41,57], HoSbTe [48], and DySbTe [50]. For selenide *Ln*SbSe compounds, metallic transport has also been observed in CeSbSe [53]. It is not clear why various transport behaviors has been observed. For example, SmSbTe show non-metallic transport but its electronic band structure probed by ARPES and first principles calculations implies that it is a metal [44]. Possible reason could be magnetic scattering and possible charge density wave due to Sb deficiency [44]. As shown in Figure 2a, the overall temperature dependence of resistivity for LaSbSe display metallic behavior with decreasing resistivity upon cooling. Despite of the metallic temperature dependence, the residual resistivity ratio *RRR*, i.e., ρ_{xx}(300 K)/ρ_{xx}(2 K), is only 1.6, which is comparable to the non-rare earth *WHM* compound ZrSnTe [58] but significantly lower than ZrSiS [21,59,60], HfSiS [61], and LaSbTe [56], implying bad metallicity for LaSbSe. In addition, resistivity for LaSbSe shows a nearly linear temperature dependence above 80 K, which is independent of the applied magnetic field [Figure 2a]. Similar near-linear resistivity has also been reported in isostructural compound CeSbSe, which is ascribed to anomalous scattering mechanism in bosonic mode [53]. Linear resistivity has also been probed in heavy fermion compounds, Fe-based superconducting metals, cuprates, and twisted bilayer graphene [62–67], which has been attributed to the presence of zero temperature instability.

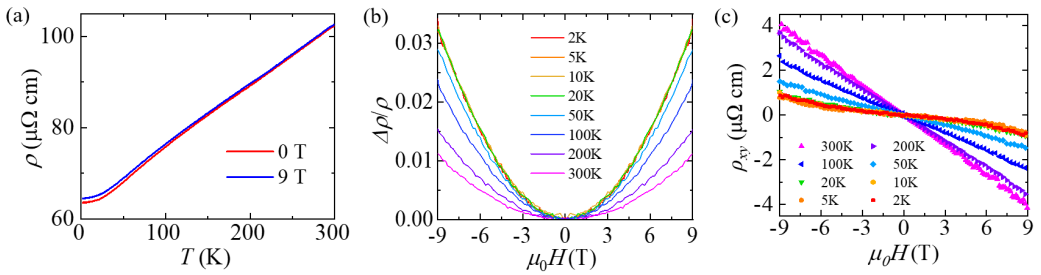

Figure 2. (**a**) Temperature dependent resistivity for LaSbSe, measured with and without applying a magnetic field of 9 T. (**b**) Normalized magnetoresistance at various temperatures for LaSbSe. (**c**) magnetic field dependent Hall resistivity at various temperatures for LaSbSe.

Many TSMs exhibit large positive magnetoresistance (MR) when magnetic field is applied perpendicular to the current direction [68], including the tetragonal non-rare

earth *WHM* [21,59–61,69] and the orthorhombic LaSbTe (space group *Pmcn*) [56] which is structurally related to the LaSbSe studied in this work. However, our LaSbSe show very small MR. Figure 2b presents the normalized MR define as $[\rho(H) - \rho(0)]/\rho(0)$, where $\rho(0)$ and $\rho(H)$ are the resistivity at zero and $\mu_0 H$ applied field, respectively [68]. LaSbSe shows weak positive MR only up to 3.3% at T = 2 K and $\mu_0 H$ = 9 T, with a nearly quadratic field dependence. The classical transport theory [70] predicts that in the small field limit, orbital MR due to Lorentz effect exhibits a parabolic field dependence and scales with the square of mobility, i.e., MR $\propto (\mu H)^2$ where μ is mobility of charge carriers. The electron-hole compensation prevents MR from saturating, which is also an important factor for large MR. To extract carrier densities and mobilities, we have performed Hall effect experiments. As shown in Figure 2c, Hall resistivity ρ_{xy} shows linear field dependence at 300 K, but deviations from linearity can be observed with decreasing temperature. Such non-linearity indicates that both electron- and hole-type carriers contribute to electronic transport in LaSbSe, which has also been observed in non-magnetic ZrSiS-type compounds [21,56,71] but is different from the linear $\rho_{xy}(H)$ seen for a few *Ln*SbTe compounds [39,44,46]. For such a multiband system, carrier densities and mobilities can be obtained by simultaneously fitting both the longitudinal resistivity $\rho_{xx}(H)$ and Hall resistivity $\rho_{xy}(H)$ to a two-band model [68]:

$$\rho_{xx} = \frac{1}{e}\left[\frac{(n_h\mu_h + n_e\mu_e) + \mu_h\mu_e(n_h\mu_e + n_e\mu_h)B^2}{(n_h\mu_h + n_e\mu_e)^2 + \mu_h{}^2\mu_e{}^2(n_h - n_e)^2B^2}\right] \quad (1)$$

$$\rho_{xy} = \frac{B}{e}\left[\frac{(n_h\mu_h{}^2 - n_e\mu_e{}^2) + \mu_h{}^2\mu_e{}^2(n_h - n_e)B^2}{(n_h\mu_h + n_e\mu_e)^2 + \mu_h{}^2\mu_e{}^2(n_h - n_e)^2B^2}\right] \quad (2)$$

where $n_{e(h)}$ and $\mu_{e(h)}$ are carrier density and mobility for electrons (holes), respectively. As shown in Figure 3a,b, the two-band model fits $\rho_{xx}(H)$ and $\rho_{xy}(H)$ very well, from which the carrier densities and the mobilities of the electron and hole bands are obtained and shown in Figure 3c,d.

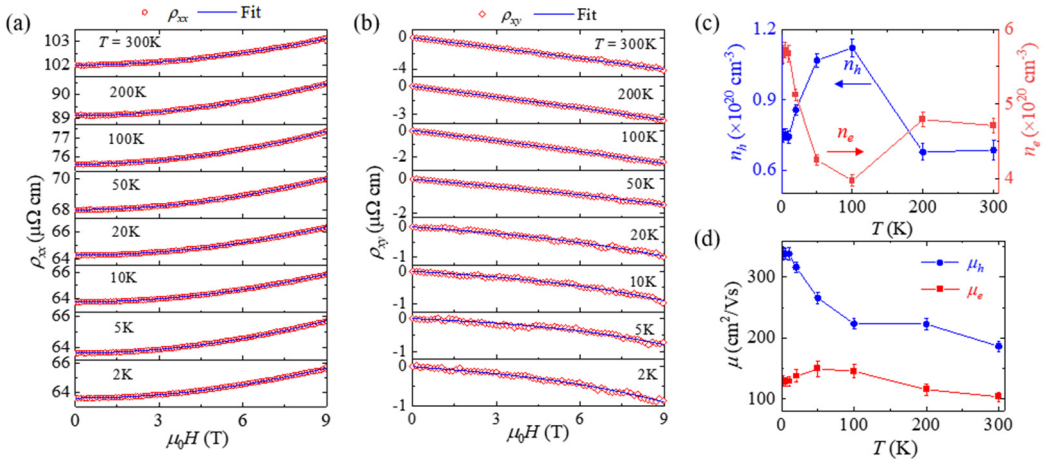

Figure 3. (**a**,**b**) Simultaneous fits for (**a**) longitudinal resistivity ρ_{xx} and (**b**) transverse resistivity ρ_{xy} using the two-band model. (**c**) Temperature dependent electron and hole carrier densities obtained from the fits. (**d**) Temperature dependent electron and hole carrier mobilities obtained from the fits.

As shown in Figure 3c, n_e and n_h are in the order of ~10^{20} cm^{-3}. Such values are comparable to *WHM*-type topological nodal-line semimetals such as ZrSi*M* (*M* = S, Si, Te). In those materials, carrier densities are lower than conventional metals but much higher than many Dirac nodal-point semimetals, which has been attributed to the nodal-line band structures that possess band crossings along a line near the Fermi level [21,71]. Nevertheless, unlike ZrSi*M* which exhibit nearly perfect electron-hole carrier compensation [21,71], n_e and n_h in LaSbSe differs a lot, by nearly an order of magnitude at T = 2 K (5.66 × 10^{20} and

7.45×10^{19} cm^{-3} for n_e and n_h, respectively). Similarly, the electron and hole mobilities are also quite different in the entire temperature range from 2 to 300 K. For example, 129 cm^2/V s for electrons and 339 cm^2/V s for holes at T = 2 K. Such values are significantly lower than LaSbTe [56] and ZrSiS [71], which is in line with the bad metallicity and small magnetoresistance for LaSbSe as stated above. As a comparison, in NdSbTe which show even lower mobility, the metallicity is fully suppressed and the material exhibits non-metallic transport behavior [46]. A comparison of different electronic properties of LaSbSe to other ZrSiS compounds are tabulated in Table 3.

Table 3. A comparison of electronic properties of LaSbSe with other ZrSiS-family compounds.

Material	Transport	MR	Carrier Density	Mobility
LaSbSe [this work]	metallic	3.3% at 2 K, 9 T	10^{19}–10^{20} cm^{-3}	100–300 cm^2/Vs
LaSbTe [56]	metallic	5×10^3% at 5 K, 9 T	10^{19} cm^{-3}	3.7×10^3–1.9×10^4 cm^2/Vs
(Zr/Hf)SiS [69,71]	metallic	8.5×10^3% at 3 K, 9 T	10^{20} cm^{-3}	1.23×10^4–1.37×10^4 cm^2/Vs
NdSbTe [46]	non-metallic	0.8 at 2 K, 9 T	10^{21} cm^{-3}	2–3 cm^2/Vs

Magnetic *Ln*SbTe compounds provide excellent platforms to investigate the new phenomena brought in by magnetic rare earth element *Ln*, such as engineering topological electronic states [28] and electron correlation enhancement [44]. For those telluride materials, non-magnetic LaSbTe provides a good reference to evaluate the effects of magnetism in those magnetic *Ln*SbTe. For example, specific heat measurement is a useful bulk measurement tool to extract information of magnetism and electronic correlations. Magnetic *Ln*SbTe compounds [39,41,44,46,48,50] display clear specific-heat anomalies around the magnetic phase transition temperatures. A few *Ln*SbTe compounds such as NdSbTe [46], SmSbTe [44] and HoSbTe [48] exhibit possible enhanced electronic correlations characterized by large Sommerfeld coefficient γ. In previous specific heat studies, LaSbTe has been used as a reference material to precisely evaluate the electronic specific heat for magnetic *Ln*SbTe because of the absence of magnetic specific heat in non-magnetic LaSbTe [44–46]. Similarly, for magnetic selenide materials *Ln*SbSe such as CeSbSe which displays interesting electronic properties such as magnetic Devil's staircase [40,53] and Kondo lattice behavior [53], the non-magnetic LaSbSe can also act as a good reference for specific heat study. In Figure 4 we present the temperature dependence of specific heat divided by temperature $C(T)/T$ for LaSbSe. Data for LaSbTe is also provided for comparison. No anomaly is seen in both compounds from 1.8 K to 30 K, consistent with their non-magnetic nature. Therefore, the total specific heat can be expressed by $C_{tot} = C_{el} + C_{ph}$, where $C_{el} = \gamma T$ is the electronic specific heat and $C_{ph} = \beta T^3$ represents the phonon contribution in the low temperature limit. This is clearly reflected by the linear dependence when plotting the low temperature C/T data against T^2, as shown in the inset of Figure 4. The linear fits yield Sommerfeld coefficients γ of 2.19 and 0.51 mJ mol/K^2 for LaSbSe and LaSbTe, respectively. Such γ values are much lower than magnetic *Ln*SbTe compounds [28,39,44,46], in which large γ above 100 mJ mol/K^2 has been observed and ascribed to the effective mass enhancement due to the presence of flat 4*f* bands near the Fermi level in the magnetically ordered state [44]. The phonon specific heat for LaSbSe and LaSbTe is very different. The fits yield β to be 2.78 and 0.39 mJ/mol K^4 for LaSbSe and LaSbTe, respectively. This leads to a Debye temperature $\theta_D = (12\pi^4 NR/5\beta)^{1/3}$ = 127.93 K for LaSbSe with an atom number per formula N = 3 and a gas constant R = 8.31 J/mol K, which is almost half of 244.53 K for LaSbTe. The suppression of θ_D for LaSbSe implies weaker interatomic interactions. Indeed, single crystals of LaSbSe are relatively softer than LaSbTe. Modification of θ_D with chalcogen substitutions Se and Te has been in seen in other materials such as Fe(Se,Te) [72–74] and ZrSi(Se,Te) [75,76], but the reported trends are not consistent. Fe(Se,Te) [72–74] shares a similar doping dependence with LaSb(Se,Te) with enhanced θ_D up on replacing Se by Te, whereas ZrSi(Se,Te) [75,76] displays an opposite trend.

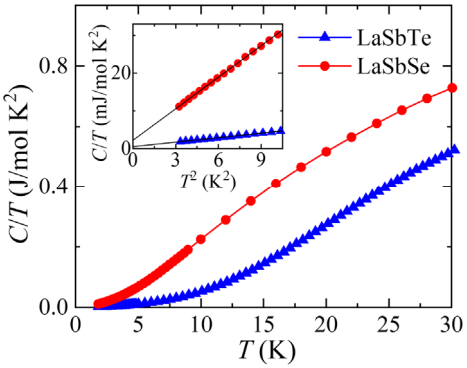

Figure 4. Temperature dependent specific heat divided by temperature C/T for LaSbSe and LaSbTe. Inset: linear fit for C/T vs. T^2 at low temperatures for LaSbSe and LaSbTe.

4. Conclusions

In conclusion, we have successfully synthesized single crystals of a new non-magnetic rare-earth compound LaSbSe. We characterized the structural, electronic transport, and thermodynamic properties. Our study reveals the metallic transport, small magnetoresistance and non-compensated charge carriers. Relatively small *RRR* and low carrier mobilities shows the bad metallicity of this compound. In addition, different Sommerfeld coefficient and Debye temperature than that of LaSbTe have been obtained through the specific heat measurement. The significantly small Sommerfeld coefficient indicates the absence of electronic correlation. Furthermore, these structural, electronic and thermodynamic properties of this compound can be tuned by studying substitution or doping study. Our results demonstrate that LaSbSe could be a non-magnetic reference material to study other magnetic compounds in the relatively under-explored *Ln*SbSe family.

Author Contributions: Single crystal growth, electronic and thermal property measurements, K.P.; Analysis, K.P. and J.H.; Powder XRD, R.B., J.S.; Single crystal XRD, L.S. and F.W.; Manuscript, K.P. and J.H. Supervision, J.H. All authors have read and agreed to the published version of the manuscript.

Funding: This work was mainly supported by the U.S. Department of Energy Office of Science under Award No. DE-SC0022006 (crystal growth and electronic, magnetic, and thermal property measurements). F. W acknowledges the support from NSF under award MRI 2117129 for single crystal XRD and structure refinements. J. S acknowledges the support from NIH under award P20GM103429 for powder XRD.

Data Availability Statement: The data presented in this study are available on request from the corresponding author.

Conflicts of Interest: The authors declare no conflict of interest.

References

1. Hasan, M.Z.; Kane, C.L. *Colloquium*: Topological insulators. *Rev. Mod. Phys.* **2010**, *82*, 3045. [CrossRef]
2. Qi, X.L.; Zhang, S.C. Topological Insulators and Superconductors. *Rev. Mod. Phys.* **2011**, *83*, 1057. [CrossRef]
3. Yan, B.; Felser, C. Topological Materials: Weyl Semimetals. *Annu. Rev. Condens. Matter Phys.* **2017**, *8*, 337. [CrossRef]
4. Armitage, N.P.; Mele, E.J.; Vishwanath, A. Weyl and Dirac semimetals in three-dimensional solids. *Rev. Mod. Phys.* **2018**, *90*, 015001. [CrossRef]
5. Bernevig, A.; Weng, H.; Fang, Z.; Dai, X. Recent Progress in the Study of Topological Semimetals. *J. Phys. Soc. Jpn.* **2018**, *87*, 041001. [CrossRef]
6. Nagaosa, N.; Morimoto, T.; Tokura, Y. Transport, magnetic and optical properties of Weyl materials. *Nat. Rev. Mater.* **2020**, *5*, 621–636. [CrossRef]
7. Fang, C.; Weng, H.; Dai, X.; Fang, Z. Topological nodal line semimetals. *Chin. Phys. B* **2016**, *25*, 117106. [CrossRef]
8. Liang, T.; Gibson, Q.; Ali, M.N.; Liu, M.; Cava, R.J.; Ong, N.P. Ultrahigh mobility and giant magnetoresistance in the Dirac semimetal Cd3As2. *Nat. Mater.* **2015**, *14*, 280. [CrossRef]
9. Fu, L. Topological Crystalline Insulators. *Phys. Rev. Lett.* **2011**, *106*, 106802. [CrossRef]
10. Li, Q.; Kharzeev, D.E.; Zhang, C.; Huang, Y.; Pletikosić, I.; Fedorov, A.V.; Zhong, R.D.; Schneeloch, J.A.; Gu, G.D.; Valla, T. Chiral Magnetic Effect in $ZrTe_5$. *Nat. Phys.* **2016**, *12*, 6. [CrossRef]

11. Jho, Y.S.; Kim, K.S. Interplay between Interaction and Chiral Anomaly: Anisotropy in the Electrical Resistivity of Interacting Weyl Metals. *Phys. Rev. B* **2013**, *87*, 205133. [CrossRef]
12. Son, D.T.; Spivak, B.Z. Chiral anomaly and classical negative magnetoresistance of Weyl metals. *Phys. Rev. B* **2013**, *88*, 104412. [CrossRef]
13. Roy, R.; Kallin, C. Collective modes and electromagnetic response of a chiral superconductor. *Phys. Rev. B* **2008**, *77*, 174513. [CrossRef]
14. Xu, S.-Y.; Liu, C.; Kushwaha, S.K.; Sankar, R.; Krizan, J.W.; Belopolski, I.; Neupane, M.; Bian, G.; Alidoust, N.; Chang, T.-R.; et al. Observation of Fermi arc surface states in a topological metal. *Science* **2015**, *347*, 294. [CrossRef] [PubMed]
15. Xu, S.-Y.; Alidoust, N.; Belopolski, I.; Yuan, Z.; Bian, G.; Chang, T.-R.; Zheng, H.; Strocov, V.N.; Sanchez, D.S.; Chang, G.; et al. Discovery of a Weyl fermion state with Fermi arcs in niobium arsenide. *Nat. Phys.* **2015**, *11*, 748–754. [CrossRef]
16. Lv, B.Q.; Weng, H.M.; Fu, B.B.; Wang, X.P.; Miao, H.; Ma, J.; Richard, P.; Huang, X.C.; Zhao, L.X.; Chen, G.F.; et al. Experimental Discovery of Weyl Semimetal TaAs. *Phys. Rev. X* **2015**, *5*, 031013. [CrossRef]
17. Huang, S.-M.; Xu, S.-Y.; Belopolski, I.; Lee, C.-C.; Chang, G.; Wang, B.; Alidoust, N.; Bian, G.; Neupane, M.; Zhang, C.; et al. A Weyl Fermion semimetal with surface Fermi arcs in the transition metal monopnictide TaAs class. *Nat. Commun.* **2015**, *6*, 7373. [CrossRef]
18. Wan, X.; Turner, A.M.; Vishwanath, A.; Savrasov, S.Y. Topological Semimetal and Fermi-Arc Surface States in the Electronic Structure of pyrochlore iridates. *Phys. Rev. B* **2011**, *83*, 205101. [CrossRef]
19. Xu, Q.; Song, Z.; Nie, S.; Weng, H.; Fang, Z.; Dai, X. Two-Dimensional Oxide Topological Insulator with Iron-Pnictide Superconductor LiFeAs Structure. *Phys. Rev. B* **2015**, *92*, 205310. [CrossRef]
20. Schoop, L.M.; Ali, M.N.; Straßer, C.; Topp, A.; Varykhalov, A.; Marchenko, D.; Duppel, V.; Parkin, S.S.; Lotsch, B.V.; Ast, C.R. Dirac Cone Protected by Non-Symmorphic Symmetry and Three-Dimensional Dirac Line Node in ZrSiS. *Nat. Commun.* **2016**, *7*, 11696. [CrossRef]
21. Hu, J.; Tang, Z.; Liu, J.; Liu, X.; Zhu, Y.; Graf, D.; Myhro, K.; Tran, S.; Lau, C.N.; Wei, J.; et al. Evidence of Topological Nodal-Line Fermions in ZrSiSe and ZrSiTe. *Phys. Rev. Lett.* **2016**, *117*, 016602. [CrossRef] [PubMed]
22. Lou, R.; Ma, J.-Z.; Xu, Q.-N.; Fu, B.-B.; Kong, L.-Y.; Shi, Y.-G.; Richard, P.; Weng, H.-M.; Fang, Z.; Sun, S.-S.; et al. Emergence of topological bands on the surface of ZrSnTe crystal. *Phys. Rev. B* **2016**, *93*, 241104. [CrossRef]
23. Neupane, M.; Belopolski, I.; Hosen, M.M.; Sanchez, D.S.; Sankar, R.; Szlawska, M.; Xu, S.-Y.; Dimitri, K.; Dhakal, N.; Maldonado, P.; et al. Observation of topological nodal fermion semimetal phase in ZrSiS. *Phys. Rev. B* **2016**, *93*, 201104. [CrossRef]
24. Takane, D.; Wang, Z.; Souma, S.; Nakayama, K.; Trang, C.X.; Sato, T.; Takahashi, T.; Ando, Y. Dirac-Node Arc in the Topological Line-Node Semimetal HfSiS. *Phys. Rev. B* **2016**, *94*, 121108. [CrossRef]
25. Hosen, M.M.; Dimitri, K.; Belopolski, I.; Maldonado, P.; Sankar, R.; Dhakal, N.; Dhakal, G.; Cole, T.; Oppeneer, P.M.; Kaczorowski, D.; et al. Tunability of the Topological Nodal-Line Semimetal Phase in ZrSiX-type materials (X = S, Se, Te). *Phys. Rev. B* **2017**, *95*, 161101. [CrossRef]
26. Chen, C.; Xu, X.; Jiang, J.; Wu, S.C.; Qi, Y.P.; Yang, L.X.; Wang, M.X.; Sun, Y.; Schröter, N.B.M.; Yang, H.F.; et al. Dirac Line Nodes and Effect of Spin-Orbit Coupling in the Nonsymmorphic Critical Semimetals. *Phys. Rev. B* **2017**, *95*, 125126. [CrossRef]
27. Hosen, M.; Dhakal, G.; Dimitri, K.; Maldonado, P.; Aperis, A.; Kabir, F.; Sims, C.; Riseborough, P.; Oppeneer, P.M.; Kaczorowski, D.; et al. Discovery of topological nodal-line fermionic phase in a magnetic material GdSbTe. *Sci. Rep.* **2018**, *8*, 13283. [CrossRef]
28. LSchoop, L.M.; Topp, A.; Lippmann, J.; Orlandi, F.; Müchler, L.; Vergniory, M.G.; Sun, Y.; Rost, A.W.; Duppel, V.; Krivenkov, M.; et al. Tunable Weyl and Dirac states in the nonsymmorphic compound CeSbTe. *Sci. Adv.* **2018**, *4*, eaar2317. [CrossRef]
29. Fu, B.-B.; Yi, C.-J.; Zhang, T.-T.; Caputo, M.; Ma, J.-Z.; Gao, X.; Lv, B.Q.; Kong, L.-Y.; Huang, Y.-B.; Richard, P.; et al. Dirac nodal surfaces and nodal lines in ZrSiS. *Sci. Adv.* **2019**, *5*, eaau6459. [CrossRef]
30. Topp, A.; Lippmann, J.M.; Varykhalov, A.; Duppel, V.; Lotsch, B.V.; Ast, C.R.; Schoop, L.M. Non-Symmorphic Band Degeneracy at the Fermi Level in ZrSiTe. *New J. Phys.* **2016**, *18*, 125014. [CrossRef]
31. Pezzini, S.; van Delft, M.R.; Schoop, L.M.; Lotsch, B.V.; Carrington, A.; Katsnelson, M.I.; Hussey, N.E.; Wiedmann, S. Unconventional mass enhancement around the Dirac nodal loop in ZrSiS. *Nat. Phys.* **2017**, *14*, 178. [CrossRef]
32. Shao, Y.; Rudenko, A.N.; Hu, J.; Sun, Z.; Zhu, Y.; Moon, S.; Millis, A.J.; Yuan, S.; Lichtenstein, A.I.; Smirnov, D.; et al. Electronic correlations in nodal-line semimetals. *Nat. Phys.* **2020**, *16*, 636. [CrossRef]
33. Hosen, M.M.; Dimitri, K.; Aperis, A.; Maldonado, P.; Belopolski, I.; Dhakal, G.; Kabir, F.; Sims, C.; Hasan, M.Z.; Kaczorowski, D.; et al. Observation of gapless Dirac surface states in ZrGeTe. *Phys. Rev. B* **2018**, *97*, 121103. [CrossRef]
34. Topp, A.; Queiroz, R.; Grüneis, A.; Müchler, L.; Rost, A.W.; Varykhalov, A.; Marchenko, D.; Krivenkov, M.; Rodolakis, F.; McChesney, J.L.; et al. Surface Floating 2D Bands in Layered Nonsymmorphic Semimetals: ZrSiS and Related Compounds. *Phys. Rev. X* **2017**, *7*, 041073. [CrossRef]
35. Liu, X.; Yue, C.; Erohin, S.V.; Zhu, Y.; Joshy, A.; Liu, J.; Sanchez, A.M.; Graf, D.; Sorokin, P.B.; Mao, Z.; et al. Quantum Transport of the 2D Surface State in a Nonsymmorphic Semimetal. *Nano Lett.* **2021**, *21*, 4887. [CrossRef]
36. Gatti, G.; Crepaldi, A.; Puppin, M.; Tancogne-Dejean, N.; Xian, L.; De Giovannini, U.; Roth, S.; Polishchuk, S.; Bugnon, P.; Magrez, A.; et al. Light-Induced Renormalization of the Dirac Quasiparticles in the Nodal-Line Semimetal ZrSiSe. *Phys. Rev. Lett.* **2020**, *125*, 076401. [CrossRef]

37. VanGennep, D.; Paul, T.A.; Yerger, C.W.; Weir, S.T.; Vohra, Y.K.; Hamlin, J.J. Possible pressure-induced topological quantum phase transition in the nodal line semimetal ZrSiS. *Phys. Rev. B* **2019**, *99*, 085204. [CrossRef]
38. Gu, C.C.; Hu, J.; Chen, X.L.; Guo, Z.P.; Fu, B.T.; Zhou, Y.H.; An, C.; Zhang, R.R.; Xi, C.Y.; Gu, Q.Y.; et al. Experimental evidence of crystal symmetry protection for the topological nodal line semimetal state in ZrSiS. *Phys. Rev. B* **2019**, *100*, 205124. [CrossRef]
39. Lv, B.; Chen, J.; Qiao, L.; Ma, J.; Yang, X.; Li, M.; Wang, M.; Tao, Q.; Xu, Z.-A. Magnetic and transport properties of low-carrier-density Kondo semimetal CeSbTe. *J. Phys. Condens. Matter* **2019**, *31*, 355601. [CrossRef]
40. Singha, R.; Salters, T.H.; Teicher, S.M.; Lei, S.; Khoury, J.F.; Ong, N.P.; Schoop, L.M. Evolving Devil's Staircase Magnetization from Tunable Charge Density Waves in Nonsymmorphic Dirac Semimetals. *Adv. Mater.* **2021**, *33*, 2103476. [CrossRef]
41. Sankar, R.; Muthuselvam, I.P.; Babu, K.R.; Murugan, G.S.; Rajagopal, K.; Kumar, R.; Wu, T.-C.; Wen, C.-Y.; Lee, W.-L.; Guo, G.-Y.; et al. Crystal Growth and Magnetic Properties of Topological Nodal-Line Semimetal GdSbTe with Antiferromagnetic Spin Ordering. *Inorg. Chem.* **2019**, *58*, 11730. [CrossRef] [PubMed]
42. Lei, S.; Saltzman, A.; Schoop, L.M. Complex Magnetic Phases Enriched by Charge Density Waves in the Topological Semimetals GdSbxTe2-x-d. *Phys. Rev. B* **2021**, *103*, 134418. [CrossRef]
43. Lei, S.; Duppel, V.; Lippmann, J.M.; Nuss, J.; Lotsch, B.V.; Schoop, L.M. Charge Density Waves and Magnetism in Topological Semimetal Candidates GdSbxTe2−x−δ. *Adv. Quantum Technol.* **2019**, *2*, 1900045. [CrossRef]
44. Pandey, K.; Mondal, D.; Villanova, J.W.; Roll, J.; Basnet, R.; Wegner, A.; Acharya, G.; Nabi, M.R.U.; Ghosh, B.; Fujii, J.; et al. Magnetic Topological Semimetal Phase with Electronic Correlation Enhancement in SmSbTe. *Adv. Quantum Technol.* **2021**, *4*, 2100063. [CrossRef]
45. Pandey, K.; Basnet, R.; Wang, J.; Da, B.; Hu, J. Evolution of Electronic and Magnetic Properties in the Topological Semimetal SmSbxTe2-x. *Phys. Rev. B* **2022**, *105*, 155139. [CrossRef]
46. Pandey, K.; Basnet, R.; Wegner, A.; Acharya, G.; Nabi, R.U.; Liu, J.; Wang, J.; Takahashi, Y.K.; Da, B.; Hu, J. Electronic and magnetic properties of the topological semimetal candidate NdSbTe. *Phys. Rev. B* **2020**, *101*, 235161. [CrossRef]
47. Sankar, R.; Muthuselvam, I.P.; Rajagopal, K.; Babu, K.R.; Murugan, G.S.; Bayikadi, K.S.; Moovendaran, K.; Wu, C.T.; Guo, G.-Y. The anisotropic magnetic properties of nonsymmorphic semi-metallic single crystal NdSbTe. *Cryst. Growth Des.* **2020**, *20*, 6585. [CrossRef]
48. Yang, M.; Qian, Y.; Yan, D.; Li, Y.; Song, Y.; Wang, Z.; Yi, C.; Feng, H.L.; Weng, H.; Shi, Y. Magnetic and electronic properties of a topological nodal line semimetal candidate: HoSbTe. *Phys. Rev. Mater.* **2020**, *4*, 094203. [CrossRef]
49. Yue, S.; Qian, Y.; Yang, M.; Geng, D.; Yi, C.; Kumar, S.; Shimada, K.; Cheng, P.; Chen, L.; Wang, Z.; et al. Topological electronic structure in the antiferromagnet HoSbTe. *Phys. Rev. B* **2020**, *102*, 155109. [CrossRef]
50. Gao, F.; Huang, J.; Ren, W.; Li, M.; Wang, H.; Yang, T.; Li, B.; Zhang, Z. Magnetic and transport properties of the topological compound DySbTe. *Phys. Rev. B* **2022**, *105*, 214434. [CrossRef]
51. Regmi, S.; Smith, R.; Sakhya, A.P.; Sprague, M.; Mondal, M.I.; Elius, I.B.; Valadez, N.; Ptok, A.; Kaczorowski, D.; Neupane, M. Observation of Gapless Nodal-Line States in NdSbTe. *arXiv* **2022**, arXiv:2210.00163.
52. Li, P.; Lv, B.; Fang, Y.; Guo, W.; Wu, Z.; Wu, Y.; Shen, D.; Nie, Y.; Petaccia, L.; Cao, C.; et al. Charge density wave and weak Kondo effect in a Dirac semimetal CeSbTe. *Sci. China Ser. G Phys. Mech. Astron.* **2021**, *64*, 237412. [CrossRef]
53. Chen, K.-W.; Lai, Y.; Chiu, Y.-C.; Steven, S.; Besara, T.; Graf, D.; Siegrist, T.; Albrecht-Schmitt, T.E.; Balicas, L.; Baumbach, R.E. Possible devil's staircase in the Kondo lattice CeSbSe. *Phys. Rev. B* **2017**, *96*, 014421. [CrossRef]
54. Petříček, V.; Dušek, M.; Palatinus, L. Crystallographic Computing System JANA2006: General features. *Z. Für Krist.-Cryst. Mater.* **2014**, *229*, 345–352. [CrossRef]
55. Ibragimova, S.G.; Aliev, F.G.; Aliev, O.M.; Mamedov, V.N.; Ibragimov, Z.A. Synthesis and properties of rare earth chalcopnictides. *Zhurnal Neorg. Khimii* **1994**, *39*, 206–207.
56. Singha, R.; Pariari, A.; Satpati, B.; Mandal, P. Magnetotransport properties and evidence of a topological insulating state in LaSbTe. *Phys. Rev. B* **2017**, *96*, 245138. [CrossRef]
57. Lei, S.; Teicher, S.M.L.; Topp, A.; Cai, K.; Lin, J.; Cheng, G.; Salters, T.H.; Rodolakis, F.; McChesney, J.L.; Lapidus, S.; et al. Band Engineering of Dirac Semimetals Using Charge Density Waves. *Adv. Mater.* **2021**, *33*, 2101591. [CrossRef]
58. Hu, J.; Zhu, Y.; Gui, X.; Graf, D.; Tang, Z.; Xie, W.; Mao, Z. Quantum oscillation evidence for a topological semimetal phase in ZrSnTe. *Phys. Rev. B* **2018**, *97*, 155101. [CrossRef]
59. Singha, R.; Pariari, A.K.; Satpati, B.; Mandal, P. Large nonsaturating magnetoresistance and signature of nondegenerate Dirac nodes in ZrSiS. *Proc. Natl. Acad. Sci. USA* **2017**, *114*, 2468. [CrossRef]
60. Ali, M.N.; Schoop, L.M.; Garg, C.; Lippmann, J.M.; Lara, E.; Lotsch, B.; Parkin, S.S.P. Butterfly magnetoresistance, quasi-2D Dirac Fermi surface and topological phase transition in ZrSiS. *Sci. Adv.* **2016**, *2*, e1601742. [CrossRef]
61. Yang, Y.; Zhu, P.; Yang, L.; Liu, J.; Li, Y.; Wang, Z. Crystal Growth and Characterization of ZrSiS-Type Topological Dirac Semimetals. *Crystals* **2022**, *12*, 728. [CrossRef]
62. Qian, B.; Tang, F.; Ruan, Y.R.; Fang, Y.; Han, Z.D.; Jiang, X.F.; Zhang, J.-M.; Chen, S.Y.; Wang, D.H. Extremely large magnetoresistance in the nonmagnetic semimetal YBi. *J. Mater. Chem. C* **2018**, *6*, 10020. [CrossRef]
63. Cha, P.; Wentzell, N.; Parcollet, O.; Georges, A.; Kim, E.A. Linear Resistivity and Sachdev-Ye-Kitaev (SYK) Spin Liquid Behavior in a Quantum Critical Metal with Spin-1/2 Fermions. *Proc. Natl. Acad. Sci. USA* **2020**, *117*, 18341. [CrossRef] [PubMed]
64. Bruin, J.A.N.; Sakai, H.; Perry, R.S.; Mackenzie, A.P. Similarity of Scattering Rates in Metals Showing T-Linear Resistivity. *Science* **2013**, *339*, 804. [CrossRef]

65. Paglione, J.; Sayles, T.A.; Ho, P.-C.; Jeffries, J.R.; Maple, M.B. Incoherent non-Fermi-liquid scattering in a Kondo lattice. *Nat. Phys.* **2007**, *3*, 703–706. [CrossRef]
66. Varma, C.M. Colloquium: Linear in Temperature Resistivity and Associated Mysteries Including High Temperature Superconductivity. *Rev. Mod. Phys.* **2020**, *92*, 031001. [CrossRef]
67. Taillefer, L. Scattering and Pairing in Cuprate Superconductors. *Annu. Rev. Condens. Matter Phys.* **2010**, *1*, 51–70. [CrossRef]
68. Hu, J.; Xu, S.-Y.; Ni, N.; Mao, Z. Transport of Topological Semimetals. *Annu. Rev. Mater. Res.* **2019**, *49*, 207. [CrossRef]
69. Kumar, N.; Manna, K.; Qi, Y.; Wu, S.C.; Wang, L.; Yan, B.; Felser, C.; Shekhar, C. Unusual Magnetotransport from Si-Square Nets in Topological Semimetal HfSiS. *Phys. Rev. B* **2017**, *95*, 121109. [CrossRef]
70. Pippard, A.B. *Magnetoresistance in Metals*; Cambridge University Press: Cambridge, UK, 1989.
71. Hu, J.; Tang, Z.; Liu, J.; Zhu, Y.; Wei, J.; Mao, Z. Nearly Massless Dirac Fermions and Strong Zeeman Splitting in the Nodal-Line Semimetal ZrSiS Probed by de Haas—Van Alphen Quantum Oscillations. *Phys. Rev. B* **2017**, *96*, 045127. [CrossRef]
72. Lin, J.Y.; Hsieh, Y.S.; Chareev, D.A.; Vasiliev, A.N.; Parsons, Y.; Yang, H.D. Coexistence of Isotropic and Extended S-Wave Order Parameters in FeSe as Revealed by Low-Temperature Specific Heat. *Phys. Rev. B* **2011**, *84*, 220507. [CrossRef]
73. Maheshwari, P.K.; Reddy, V.R.; Awana, V.P.S. Heat Capacity and Mössbauer Study of Self-Flux Grown FeTe Single Crystal. *J. Supercond. Nov. Magn.* **2018**, *31*, 1659. [CrossRef]
74. Chen, G.Y.; Zhu, X.; Yang, H.; Wen, H.H. Highly Anisotropic Superconducting Gaps and Possible Evidence of Antiferromagnetic Order in FeSe Single Crystals. *Phys. Rev. B* **2017**, *96*, 064524. [CrossRef]
75. Song, J.; Song, M.; Li, Z.; Wang, J.; Wang, Y.; Zhang, L.; Han, Y.; Cao, L.; Xiong, Y.; Liu, D. Signatures of Fermi Surface Topology Change in the Nodal-Line Semimetal ZrSiSe1-xTex. *Phys. Rev. B* **2021**, *103*, 165141. [CrossRef]
76. Sankar, R.; Peramaiyan, G.; Muthuselvam, I.P.; Butler, C.; Dimitri, K.; Neupane, M.; Rao, G.N.; Lin, M.-T.; Chou, F.C. Crystal growth of Dirac semimetal ZrSiS with high magnetoresistance and mobility. *Sci. Rep.* **2017**, *7*, 40603. [CrossRef] [PubMed]